

Atomically Dispersed Pt–N<sub>3</sub>C<sub>1</sub> Sites Enabling Efficient and Selective Electrocatalytic C–C Bond Cleavage in Lignin Models under Ambient ConditionsTingting Cui,<sup>¶</sup> Lina Ma,<sup>¶</sup> Shibin Wang,<sup>¶</sup> Chenliang Ye, Xiao Liang, Zedong Zhang, Ge Meng, Lirong Zheng, Han-Shi Hu, Jiangwei Zhang,\* Haohong Duan,\* Dingsheng Wang,\* and Yadong LiCite This: *J. Am. Chem. Soc.* 2021, 143, 9429–9439

Read Online

ACCESS |



Metrics &amp; More

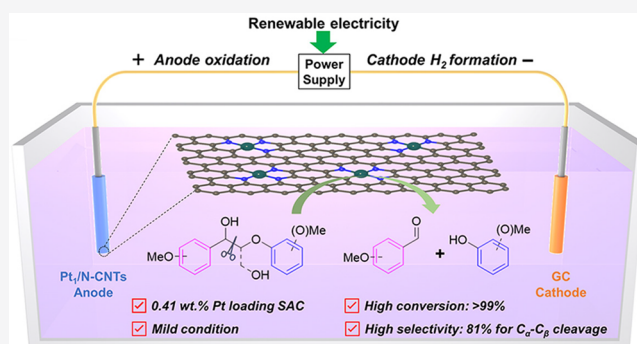


Article Recommendations



Supporting Information

**ABSTRACT:** Selective cleavage of C–C linkages is the key and a challenge for lignin degradation to harvest value-added aromatic compounds. To this end, electrocatalytic oxidation presents a promising technique by virtue of mild reaction conditions and strong sustainability. However, the existing electrocatalysts (traditional bulk metal and metal oxides) for C–C bond oxidative cleavage suffer from poor selectivity and low product yields. We show for the first time that atomically dispersed Pt–N<sub>3</sub>C<sub>1</sub> sites planted on nitrogen-doped carbon nanotubes (Pt<sub>1</sub>/N-CNTs), constructed via a stepwise polymerization–carbonization–electrostatic adsorption strategy, are highly active and selective toward C<sub>α</sub>–C<sub>β</sub> bond cleavage in β-O-4 model compounds under ambient conditions. Pt<sub>1</sub>/N-CNTs exhibits 99% substrate conversion with 81% yield of benzaldehyde, which is exceptional and unprecedented compared with previously reported electrocatalysts. Moreover, Pt<sub>1</sub>/N-CNTs using only 0.41 wt % Pt achieved a much higher benzaldehyde yield than those of the state-of-the-art bulk Pt electrode (100 wt % Pt) and commercial Pt/C catalyst (20 wt % Pt). Systematic experimental investigation together with density functional theory (DFT) calculation suggests that the superior performance of Pt<sub>1</sub>/N-CNTs arises from the atomically dispersed Pt–N<sub>3</sub>C<sub>1</sub> sites facilitating the formation of a key C<sub>β</sub> radical intermediate, further inducing a radical/radical cross-coupling path to break the C<sub>α</sub>–C<sub>β</sub> bond. This work opens up opportunities in lignin valorization via a green and sustainable electrochemical route with ultralow noble metal usage.



## 1. INTRODUCTION

Lignin is an abundant, low-cost, and underutilized renewable biomass. Its valorization to produce fuels and small molecular aromatic compounds is a promising strategy to diminish reliance on fossil fuel resources.<sup>1</sup> However, this is severely hindered by its recalcitrant polymeric structures consisting of methoxylated phenylpropane subunits connected through various C–O and C–C linkages.<sup>2</sup> Particularly, C–C bonds generally have higher dissociation energy than those of C–O bonds in lignin, rendering selective cleavage of C–C bonds the key and a challenge for lignin degradation. In this regard, several strategies including hydrolysis, pyrolysis, reduction, and oxidation have been developed.<sup>3,4</sup> Among these, selective catalytic oxidation has attracted most of the attention since oxidation could cleave the C–C linkage while preserving the aromatic ring structure, transforming lignin into highly functionalized monomeric aromatic compounds, such as phenolic aldehydes, ketones, acids, and acid derivative products, which can be used directly as fine chemicals or as platform chemicals.<sup>5</sup> The oxidative depolymerization of lignin has been under investigation since the first half of the last

century.<sup>6,7</sup> A series of homogeneous and heterogeneous catalytic systems have been reported with promising conversion and C–C bond cleavage selectivity for lignin model compounds under thermal conditions.<sup>8–13</sup> However, these conventional thermal catalytic processes have encountered the drawbacks of harsh reaction conditions like elevated temperature and pressure, requirements for costly catalysts, as well as sometimes a long reaction time, which may hinder large-scale applications.<sup>14</sup> Therefore, it is highly appealing to develop efficient alternative strategies for the selective oxidative cleavage of the C–C bond within lignin under mild conditions.

Electrocatalytic oxidation is a potentially promising technique for lignin depolymerization.<sup>15–18</sup> It features eminent

Received: March 1, 2021

Published: June 17, 2021



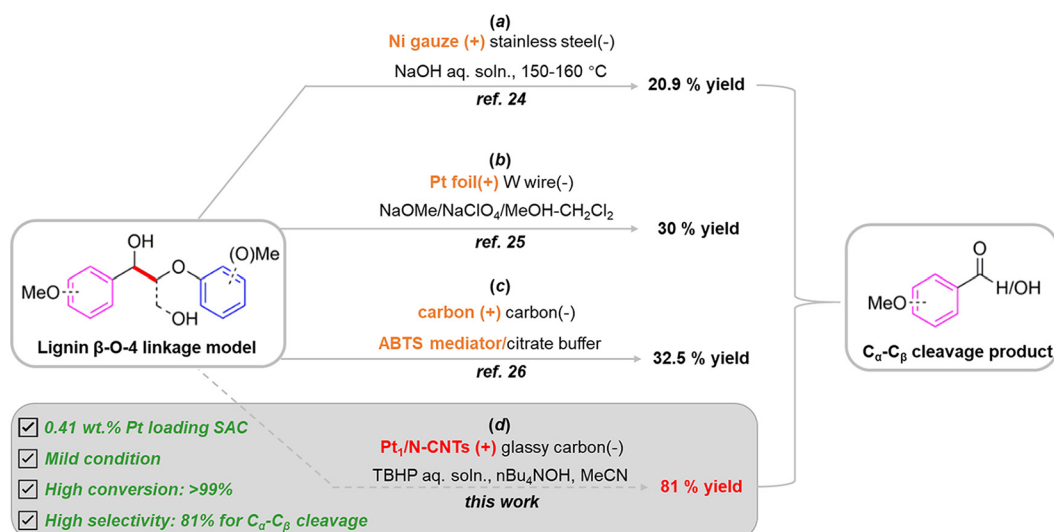


**Figure 1.** Electrocatalytic oxidation cleavage of the C<sub>α</sub>-C<sub>β</sub> bond in lignin β-O-4 model compounds. (a)–(c) Previously reported electrocatalytic systems, including bulk Ni, Pt, and carbon electrode combined with ABTS mediator. (d) We show in this work the highly efficient and selective C<sub>α</sub>-C<sub>β</sub> bond oxidative cleavage using the Pt<sub>1</sub>/N-CNTs electrocatalyst under ambient conditions.

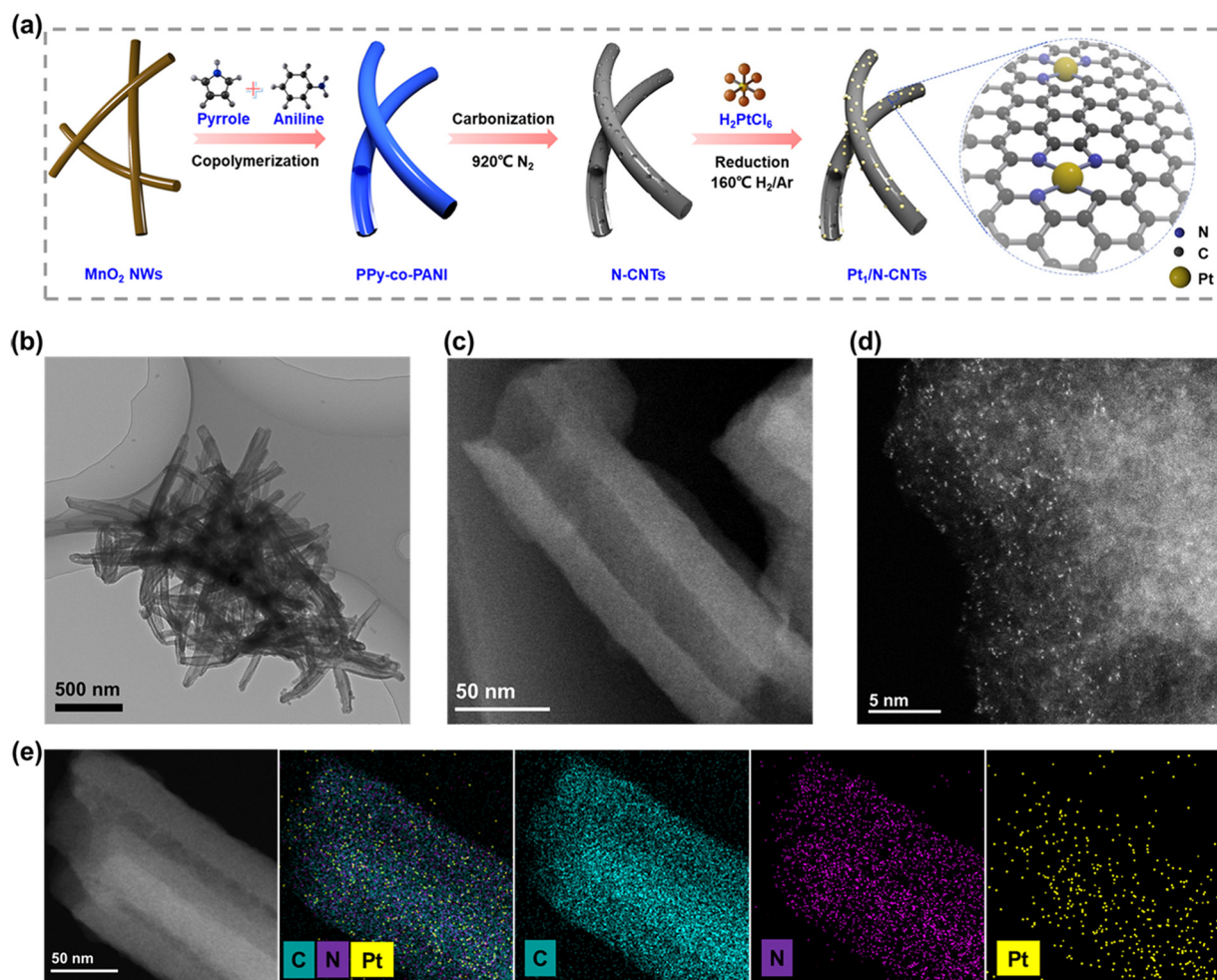


**Figure 2.** Synthetic strategy and characterization of the Pt<sub>1</sub>/N-CNTs catalyst. (a) Schematic illustration of the preparation of Pt<sub>1</sub>/N-CNTs. (b) TEM image of Pt<sub>1</sub>/N-CNTs. (c) HAADF-STEM image of Pt<sub>1</sub>/N-CNTs. (d) Representative AC HAADF-STEM image of Pt<sub>1</sub>/N-CNTs. (e) EDX elemental mapping analysis of Pt<sub>1</sub>/N-CNTs.

advantages over conventional thermocatalytic processes, such as mild reaction conditions, enhanced sustainability by

utilization of renewable electricity as a power source, and the simultaneous generation of valuable H<sub>2</sub> at the cathode as a

supererogatory product.<sup>19–21</sup> Nevertheless, research on electrocatalytic lignin oxidation is still at the infancy stage, especially for selective C–C bond cleavage.<sup>22,23</sup> Pardini and co-workers first reported electrocatalytic oxidation of a lignin  $\beta$ -O-4 dimeric model compound targeting  $C_\alpha$ – $C_\beta$  bond cleavage using bulk Ni electrode at 150–160 °C, but only 20.9% yield of the  $C_\alpha$ – $C_\beta$  bond cleaved products (aromatic aldehyde and carboxylic acid) was obtained (Figure 1a).<sup>24</sup> Later, they further found that when utilizing Pt foil as the anode,  $C_\alpha$ – $C_\beta$  bond oxidative cleavage could proceed at ambient temperature while delivering an improved yield of aromatic aldehyde (Figure 1b).<sup>25</sup> Alternatively, Rochefort and co-workers described an indirect electrooxidation methodology by using 2,2'-azino-bis(3-ethylbenzthiazoline-6-sulfonate) (ABTS) as a redox mediator to facilitate  $C_\alpha$ – $C_\beta$  bond cleavage. A slightly higher yield of aldehyde product (32.5%) was reported in this system (Figure 1c).<sup>26</sup> In addition, a series of metal oxides ( $PbO_2$ <sup>27–33</sup> and  $TiO_2$ <sup>34</sup>) and mixed metal oxides based on precious metals ( $RuO_2$ <sup>35–41</sup> and  $IrO_2$ <sup>35,37–41</sup>) were also reported for native and technical lignin depolymerization. However, these catalysts suffered from poor selectivity, resulting in highly complex product mixtures.<sup>27,28,33,36,39–46</sup> The lack of selectivity and low product yields represent the critical bottlenecks in the electrocatalytic lignin oxidation process. In this context, developing a catalyst that can effectively steer  $C_\alpha$ – $C_\beta$  bond selective cleavage is highly desired but challenging.

Recently, single-atom catalysts (SACs), referring to heterogeneous catalysts comprised of spatially isolated metal atoms stabilized by neighboring surface atoms such as carbon, nitrogen, or oxygen, etc., on appropriate hosts, have stood out and become a brand-new research frontier in heterogeneous catalysis.<sup>47,48</sup> They possess well-defined active centers with 100% atomic utilization in theory. Moreover, SACs usually exhibit unique electronic structures due to unsaturated coordinated environments, strong metal support interactions, and quantum size effects.<sup>49</sup> Thus, relative to nanoscale metal counterparts, SACs often give rise to a different reaction pathway, leading to superior catalytic performance, as has been demonstrated in various thermocatalysis,<sup>50–57</sup> photocatalysis,<sup>58–61</sup> and electrocatalysis.<sup>62–65</sup> Moreover, given the highly uniform active sites brought about by similar spatial and electronic interaction with substrates, SACs have tremendous potential to enhance the selectivity in lignin electrochemical oxidative cleavage. However, to the best of our knowledge, SACs have never been exploited as an electrocatalyst for lignin oxidation.

Intrigued by the merits of SACs and scanty research on electrocatalytic C–C bond cleavage, herein we design a single-atom Pt catalyst anchored on N-doped carbon nanotubes ( $Pt_1/N$ -CNTs) for selective  $C_\alpha$ – $C_\beta$  bond cleavage. The atomic structure was carefully examined by aberration-corrected high-angle annular dark-field scanning transmission electron microscopy (AC HAADF-STEM) and X-ray absorption spectroscopy (XAS), revealing isolated sites with the  $Pt-N_3C_1$  configuration.  $Pt_1/N$ -CNTs exhibits unprecedented high  $C_\alpha$ – $C_\beta$  bond cleavage activity and selectivity in  $\beta$ -O-4 model compounds under ambient conditions, achieving 99% conversion and 81% C–C bond cleavage selectivity, which greatly exceed previously reported electrocatalysts. Moreover,  $Pt_1/N$ -CNTs using only 0.41 wt % Pt achieved a much higher benzaldehyde yield than those of the state-of-the-art bulk Pt electrode (100 wt % Pt) and commercial Pt/C catalyst (20 wt

% Pt). The reaction mechanism was revealed by radical trapping, isotope labeling, as well as DFT calculations. The strategy of constructing single-site active centers with unique configuration represents a significant advance in boosting  $C_\alpha$ – $C_\beta$  bond cleavage while reducing the noble metal usage.

## 2. RESULTS AND DISCUSSION

**2.1. Synthesis and Structural Characterizations of the  $Pt_1/N$ -CNTs Catalyst.** The  $Pt_1/N$ -CNTs catalyst was fabricated via a facile three-step strategy as illustrated in Figure 2a. First, the carbon-based conjugated polymer precursors (PPy-co-PANI) were constructed by copolymerization of pyrrole and aniline using  $MnO_2$  nanowires (Figure S1) as the oxidant and reactive template<sup>66,67</sup> (Step 1). Notably, the redox potential of  $MnO_2$  (1.224 V vs SHE for  $MnO_2/Mn^{2+}$ )<sup>68</sup> is higher than the redox polymerization potential of pyrrole and aniline (<0.7 V vs SHE).<sup>69</sup> Thus,  $MnO_2$  could effectively initiate the polymerization of monomers. Furthermore,  $MnO_2$  nanowires also acted as the template for the growth of PPy-co-PANI since the polymerization occurred at the  $MnO_2$ /monomers interface. During this process,  $MnO_2$  was consumed via the reaction of  $MnO_2 + 4H^+ + 2e^- \rightarrow Mn^{2+} + 2H_2O$ ,<sup>70</sup> consequently leading to the formation of hollow-structured PPy-co-PANI. Then the resultant PPy-co-PANI was converted into N-CNTs via carbonization at 920 °C under  $N_2$  atmosphere (Step 2). The transmission electron microscopy (TEM) images in Figure S2 clearly show that N-CNTs possess a well-defined hollow cavity with an outer diameter of 40–70 nm and length of 0.2–1  $\mu m$ . Note that abundant micropores with sizes of 0.5 and 1.2 nm were generated across the CNT walls during carbonization (Figure S3), benefiting from the robust framework of PPy-co-PANI. A high N-doping level of 7.8 wt % was achieved in N-CNTs as revealed by X-ray photoelectron spectroscopy (XPS) characterization. In addition, N-CNTs exhibit a much higher D/G intensity ratio ( $I_D/I_G$ ) of 3.5 than that of commercial CNTs (0.15) in the Raman spectra (Figure S4), indicating the presence of numerous defects on the walls, which may be caused by the microporous structure and abundant N-doping.<sup>71–73</sup> The content of residual Mn in N-CNTs is 0.0033 wt % as determined by inductively coupled plasma-optical emission spectrometry (ICP-OES). Afterward,  $Pt^{4+}$  species were uniformly deposited on N-CNTs via electrostatic adsorption, and the composites were reduced at 160 °C in 5 vol %  $H_2/Ar$  atmosphere for 0.5 h, through which the  $Pt_1/N$ -CNTs catalyst was produced (Step 3) (for more details, see the Supporting Information).

TEM and HAADF-STEM images reveal that there are no Pt NPs or small clusters throughout the entire region of the sample (Figure 2b, c). This is also in good agreement with the absence of obvious diffraction peaks of Pt in the X-ray diffraction (XRD) profile (Figure S5). Energy-dispersive X-ray spectroscopy (EDS) mapping (Figure 2e) shows a homogeneous distribution of C, N, and Pt. To identify the dispersion status of Pt species on N-CNTs at the atomic scale, subangstrom resolution HAADF-STEM was used. As shown in Figure 2d, a large number of ultrasmall white dots (~1–2 Å) are densely planted on N-CNTs, ascribable to single Pt atoms on account of the atomic number contrast in the image (Figure S6). By further examining numerous low/high-magnification HAADF-STEM images obtained from different regions of the sample, we concluded that the as-synthesized  $Pt_1/N$ -CNTs contained only isolated Pt atoms. The Pt loading amount was determined to be 0.41 wt % by ICP-OES analysis.



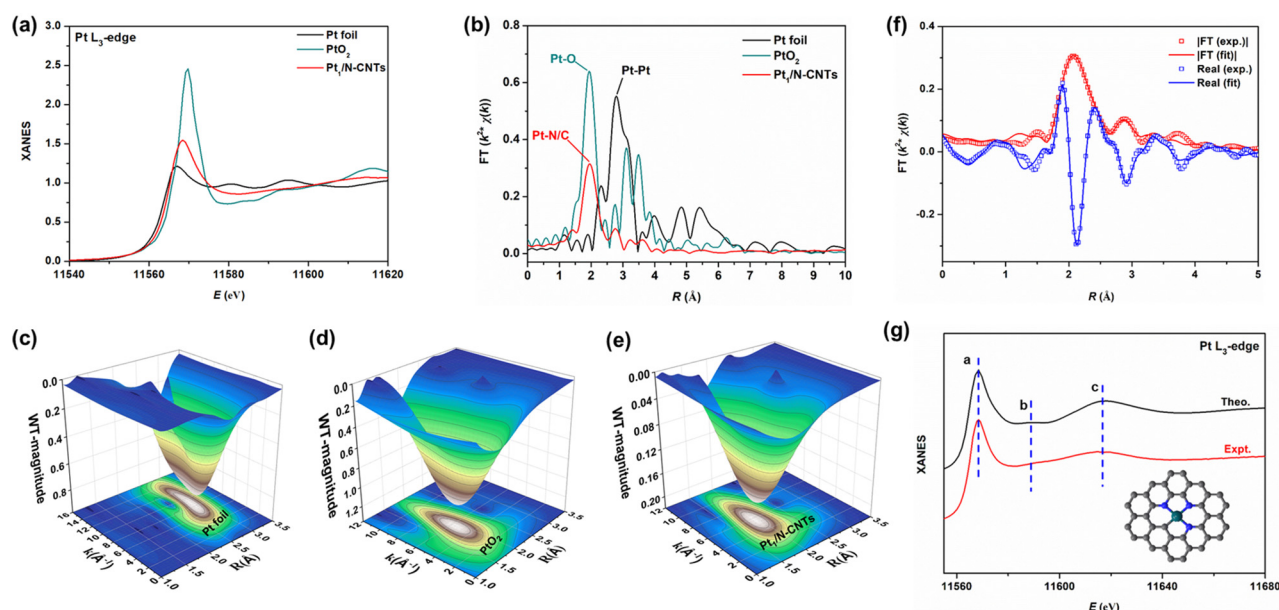


**Figure 3.** Structural identification of a Pt single atom in the Pt<sub>1</sub>/N-CNTs catalyst. (a) The Pt L<sub>3</sub>-edge XANES spectra of Pt<sub>1</sub>/N-CNTs (red), along with Pt foil (black) and PtO<sub>2</sub> (cyan) for comparison. (b) FT of the *k*<sup>2</sup>-weighted EXAFS spectra of Pt<sub>1</sub>/N-CNTs (red), along with reference samples Pt foil (black) and PtO<sub>2</sub> (cyan). WT for the *k*<sup>2</sup>-weighted EXAFS signals of (c) Pt foil, (d) PtO<sub>2</sub>, and (e) Pt<sub>1</sub>/N-CNTs. (f) FT of the *k*<sup>2</sup>-weighted EXAFS spectrum and fit in *R* space of Pt<sub>1</sub>/N-CNTs with the magnitude (red) and real component (blue). (g) Comparison between the experimental Pt L<sub>3</sub>-edge XANES spectrum of Pt<sub>1</sub>/N-CNTs and the theoretical spectrum calculated for Pt–N<sub>3</sub>C<sub>1</sub>. The FT are corrected for the phase shift.

By contrast, isolated Pt atoms as well as well-crystalline particles of 1–2.5 nm were formed when commercial CNTs were used as the support with a similar Pt loading amount (Figure S7 and Table S1), and the resulting sample was denoted as Pt<sub>1+NPs</sub>/CNTs. This result highlights the distinct superiority of N-CNTs in anchoring single atoms by high-level N-doping and abundant micropores on the walls. In addition, another control sample, consisting of 0.44 wt % Pt NPs on N-CNTs (Pt NPs/N-CNTs), was also prepared by mixing Pt NPs of 2.5–5 nm with N-CNTs for investigating the effect of the Pt states on the catalytic performance (Figure S8).

The electronic structures of C and N species in Pt<sub>1</sub>/N-CNTs were detected by XPS and synchrotron-based soft X-ray absorption near-edge structure (XANES) spectroscopy. As shown in Figure S9, the N 1s high-resolution XPS spectrum can be well fitted with three peaks at the binding energies of 398.5, 401.0, and 403.7 eV, assigned to pyridinic-N, graphitic-N, and oxidized-N, respectively (Table S2). In good accordance with the XPS result, three N 1s– $\pi^*$  transitions peaks (N1, N2, N3) corresponding to pyridine-like, graphite-like, and NO structures were found in the N K-edge XANES spectrum (Figure S10).<sup>74</sup> Notably, the relative intensity of peak N1 in Pt<sub>1</sub>/N-CNTs is obviously weaker than that of N-CNTs, suggesting that Pt single atoms are trapped at pyridine-like N sites, highlighting the anchoring effect of pyridinic-N for single atoms. The C K-edge spectrum of Pt<sub>1</sub>/N-CNTs showed three obvious peaks at 286.0 eV (peak A), 289.1 eV (peak B), and 292.7 eV (peak C), which derive from the dipole transition of the C 1s core electron into the antibonding orbitals of  $\pi^*$  C=C, mixed states of  $\pi^*$  and  $\sigma^*$  C–N/O, and  $\sigma^*$  C–C,<sup>75</sup> respectively (Figure S11). No obvious change can be observed in the C K-edge spectra during deposition of Pt SAs on N-CNTs.

The chemical state of Pt SAs in Pt<sub>1</sub>/N-CNTs was examined by XPS. In Figure S12, we present the Pt 4f XPS spectra of

Pt<sub>1</sub>/N-CNTs as well as those of Pt NPs/N-CNTs and Pt<sub>1+NPs</sub>/CNTs for comparison. Pt<sub>1</sub>/N-CNTs exhibits a single doublet (4f<sub>7/2</sub> and 4f<sub>5/2</sub>) at 72.9 and 76.2 eV, implying that Pt exhibits the valence state close to +2. In contrast, two sets of peaks for Pt<sub>1+NPs</sub>/CNTs can be observed with 4f<sub>7/2</sub> at 71.5 and 73.1 eV, which can be assigned to Pt<sup>0</sup> and Pt <sup>$\delta^+$</sup>  ( $2 < \delta < 4$ ), respectively, due to the coexistence of NPs and SAs.<sup>76</sup> Pt NPs/N-CNTs consists almost entirely of Pt<sup>0</sup> species with a small contribution from Pt<sup>2+</sup> due to the surface oxidation of NPs. In order to decode the electronic structure and coordination configuration of Pt, XANES and extended X-ray absorption fine structure (EXAFS) spectroscopy measurements were performed at the Pt L<sub>3</sub>-edge. In the XANES spectra, the intensity of the white line peak of Pt species in Pt<sub>1</sub>/N-CNTs is much lower than that of PtO<sub>2</sub> but higher than that of metallic Pt foil (Figure 3a), indicating that the Pt species in Pt<sub>1</sub>/N-CNTs exhibit a positive valence, which is well consistent with the XPS result. Figure 3b shows the phase-corrected Fourier transform (FT) curves at the *R* space of the Pt L<sub>3</sub>-edge EXAFS spectra for Pt<sub>1</sub>/N-CNTs in comparison with the references of Pt foil and PtO<sub>2</sub>. Notably, *k*<sup>2</sup>-weighted FT was adopted to achieve an intuitive comparison between different samples. Pt<sub>1</sub>/N-CNTs has a dominant peak at 1.95 Å corresponding to the Pt–N/C scattering path with the absence of a peak at 2.78 Å from Pt–Pt contribution, categorically confirming the isolated state of Pt atoms, consistent with the HAADF-STEM observation. EXAFS wavelet transform (WT) analysis, which can provide not only radial distance resolution but also *k*-space resolution, was employed for further investigation of the coordination conditions of Pt centers in Pt<sub>1</sub>/N-CNTs (Figure 3c–e). A WT intensity maximum near 5.7 Å<sup>−1</sup> arising from the light atom coordinator is well resolved at 1.95 Å for Pt<sub>1</sub>/N-CNTs, whereas an intensity maximum at 8.5 Å<sup>−1</sup> associated with the Pt–Pt coordination was not detected. This result not only further confirms that Pt exists as a mononuclear center in the

Table 1. Catalytic Conversion of 2-Phenoxy-1-phenylethanol over Different Catalysts<sup>a</sup>

entry	catalyst	Pt loading amount (wt %) <sup>b</sup>	conversion 1a (%) <sup>c</sup>	product yield (%) <sup>c</sup>		
				2a	3a	4a
1	N-CNTs	0	<10	ND	ND	ND
2	Pt NPs/N-CNTs	0.44	62	<5	25	12
3	Pt <sub>1+NP</sub> /CNTs	0.38	77	ND	36	21
4	Pt <sub>1</sub> /N-CNTs	0.41	99	<5	81	56
5 <sup>d</sup>	Pt/C	20	21	ND	19	11
6 <sup>e</sup>	Pt/C	20	100	ND	55	35
7	Pt electrode	100	88	ND	55	<5

<sup>a</sup>Reaction conditions: **1a** (0.1 mmol), *n*Bu<sub>4</sub>NOH (0.2 mmol), TBHP (0.5 mmol), MeCN (1.0 mL), RT, 5 h, under air, electrolysis under current of 20 mA and potential of 5.0 V vs Ag/AgCl, unless otherwise noted. Catalyst loading on GCE of 0.5 mg/cm<sup>2</sup>. Glassy carbon (GC) as the counter electrode. Ag/AgCl as the reference electrode. <sup>b</sup>Pt loading amounts in the catalysts were determined by ICP-OES. <sup>c</sup>Conversions of substrates were determined by <sup>1</sup>H NMR using CH<sub>2</sub>Br<sub>2</sub> as an internal standard. Yields of products were the isolated yields. <sup>d</sup>The mass loading of Pt on the GCE was kept the same as entry 4. <sup>e</sup>The mass loading of the total catalyst on the GCE was kept the same as entry 4.

absence of metallic Pt species in Pt<sub>1</sub>/N-CNTs but also substantiates the assignment of the major peak at ~1.95 Å to Pt–C/N bonding. We also carried out least-squares EXAFS fitting analysis to extract quantitative structural results for the Pt moiety in Pt<sub>1</sub>/N-CNTs. The best-fitting analysis reveals that each Pt atom is coordinated with one C atom (CN = 0.9) and three N atoms (CN = 3.1) at distances of 1.92 and 1.99 Å, respectively (Figure 3f, Figure S14, and Table S3). Considering that the XANES spectrum possesses higher sensitivity to the local coordination environment of the absorbing species, XANES simulations were further carried out. Different structure models with various Pt–N/C coordinating conditions were established by DFT calculations (Figure S15), and the corresponding XANES spectra were calculated. As shown in Figure 3g, the simulated spectrum based on the proposed Pt–N<sub>3</sub>C<sub>1</sub> model can well reproduce the experimental XANES features of Pt<sub>1</sub>/N-CNTs. Moreover, the average Pt–C and Pt–N bond lengths predicted by DFT are 1.92 and 1.97 Å, respectively, which are close to the structural parameters given by EXAFS fitting (Table S3). However, the calculated spectra for the structures of Pt–N<sub>4</sub>, Pt–N<sub>1</sub>C<sub>3</sub>, Pt–N<sub>2</sub>C<sub>2</sub>-1, and Pt–N<sub>2</sub>C<sub>2</sub>-2 models, which exhibit either more positive or more negative absorption edges than the experimental result, are distinctly different (Figure S16). Taken together, the combination of EXAFS and XANES results clearly revealed the formation of isolated Pt–N<sub>3</sub>C<sub>1</sub> moieties in Pt<sub>1</sub>/N-CNTs. Additionally, spin-polarized calculations further reveal that the Pt atom in the Pt–N<sub>3</sub>C<sub>1</sub> model exhibits a very low magnetic momentum value of 0.02 μ<sub>B</sub>, and the Bader charge value of the Pt atom was calculated to be +0.57 |e|, suggesting that the Pt valence state is close to +2 with an electronic configuration of 6s<sup>0</sup>5d<sup>8</sup>, which is well consistent with the above experimental evidence.

**2.2. Electrocatalytic Oxidation of 2-Phenoxy-1-phenylethanol.** To study the C–C bond cleavage regularity of the as-prepared Pt–N<sub>3</sub>C<sub>1</sub> catalyst, a representative β-O-4 dimeric model compound, 2-phenoxy-1-phenylethanol (**1a**), containing C<sub>α</sub>–OH, C<sub>α</sub>–C<sub>β</sub>, and C<sub>β</sub>–O bonds, was used as the substrate in this study. Bulk electrolysis of **1a** at the anode was performed using *tert*-butyl hydroperoxide<sup>77</sup> (TBHP, 70% aq. soln) as the oxidant under a constant current of 20 mA for 5 h

along with H<sub>2</sub> generation at the cathode under ambient conditions. Results with different catalysts for catalytic oxidation of **1a** are summarized in Table 1. For the support N-CNTs only, there was hardly any activity toward the conversion of the substrate (less than 10%, Table 1, entry 1), indicating that the residuary trace Mn is inactive for this reaction. When loading 0.44 wt % Pt NPs on N-CNTs (Pt NPs/N-CNTs), a medium activity with 62% conversion of **1a** (Table 1, entry 2) was detected. However, the yield of the desired product of benzaldehyde (**3a**) from C<sub>α</sub>–C<sub>β</sub> bond oxidative cleavage is very low. When Pt<sub>1+NP</sub>/CNTs was used, which contains both Pt SAs and NPs, with a total Pt loading of 0.38 wt %, the conversion was promoted to 77% with a higher yield of 36% for **3a** (Table 1, entry 3). This result suggests the prominent advantage of Pt SAs over NPs in oxidative cleavage of **1a**. Inspired by this, we further examined the performance of Pt<sub>1</sub>/N-CNTs, which contains only SA Pt with 0.41 wt % loading under the same conditions. To our delight, Pt<sub>1</sub>/N-CNTs catalyst confers remarkably higher activity than Pt NPs/N-CNTs and Pt<sub>1+NP</sub>/CNTs, achieving 99% substrate conversion with 81% yield and 5.6% faradaic efficiency for **3a**, further corroborating the superior catalytic performance of the Pt SAs (Table 1, entry 4). In addition, we also investigated the catalytic performance of the benchmark commercial Pt/C catalyst decorated with 20 wt % Pt NPs. As shown in Table 1, entry 5, Pt/C only delivered a conversion of 21% with 19% yield of **3a** when the Pt loading amount on the glassy carbon electrode (GCE) was kept the same as for Pt<sub>1</sub>/N-CNTs. Even in the case of the same catalyst loading as Pt<sub>1</sub>/N-CNTs on GCE, Pt/C still exhibited a much lower yield of 55% for **3a**, although its conversion was good enough (Table 1, entry 6). It is worth noting that the Pt<sub>1</sub>/N-CNTs catalyst even has a significant advantage over the bulk Pt electrode with 100% Pt content, which delivered a much lower yield of 55% for **3a** (Table 1, entry 7). Compared with previously reported electrocatalytic systems (Figure 1), an overwhelming advantage for Pt<sub>1</sub>/N-CNTs can be seen. We further compared the catalytic performance of Pt<sub>1</sub>/N-CNTs with previously reported typical thermocatalytic and photocatalytic systems (Table S4). Apparently, the present Pt<sub>1</sub>/N-CNTs electrocatalyst surpasses most of the previously reported catalytic systems in terms of

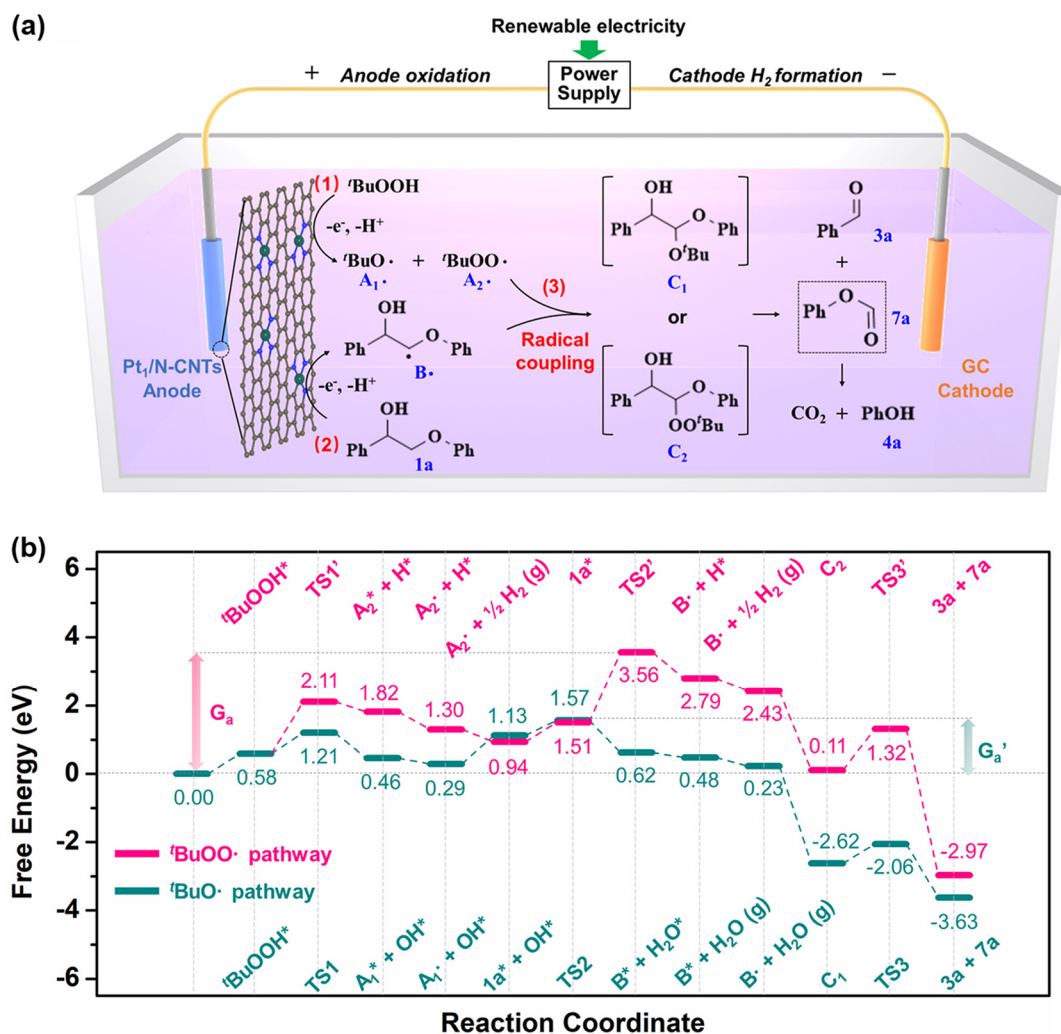


**Figure 4.** Reaction pathway based on experiments and DFT calculations. (a) Proposed mechanism of Pt<sub>1</sub>/N-CNTs-catalyzed conversion of 1a. (b) DFT-calculated potential energy surface for 1a conversion on the Pt<sub>1</sub>/N-CNTs surface.

$C_{\alpha}$ – $C_{\beta}$  bond cleavage performance (i.e., the yield of 3a, 5a, and 6a). Furthermore, from the point of energy utilization, the electrocatalytic process is more sustainable than the traditional one by virtue of direct integration with renewable energy. Notably, the high-temperature electrocatalytic process deserves further exploration to achieve energy integration with lignin pretreatment processes as well. On the other hand, considering the challenge associated with the separation of lignin cleavage products, the oxygen-containing aromatics obtained here may be further upgraded via hydrodeoxygenation to aromatic hydrocarbons and used directly as biofuels. Alternatively, convergent transformation of lignin derivatives into a relatively single commodity via the funneling approach is also viable to fundamentally solve the separation issue, as we reported in another work recently.<sup>78</sup>

To investigate the generality of the Pt<sub>1</sub>/N-CNTs catalyst, a variety of lignin model compounds with different substituents were evaluated (Table S5). It is known that  $\beta$ -O-4 dimeric model compounds with methoxy groups are structurally closer to the true nature lignin, which may affect the activation of the  $C_{\alpha}$ – $C_{\beta}$  bond. The catalytic oxidative cleavage of the  $\beta$ -O-4 compound with methoxy groups in both benzene rings (red and blue colored part) over Pt<sub>1</sub>/N-CNTs was investigated (Table S5, entry 1). The substrate was nearly completely

converted, producing the corresponding aldehyde in a moderate yield. It has been reported that the  $C_{\gamma}$ –OH will make the  $C_{\alpha}$ – $C_{\beta}$  bond more resistant to oxidation.<sup>79</sup> Hence, lignin models with  $C_{\gamma}$ –OH were also investigated. Moderate to high yields of aromatic aldehydes were obtained under the present mild conditions (Table S5, entries 2, 3). In addition, electrocatalytic oxidation of more challenging  $\beta$ -1 models with different substituents such as methoxy, halogen, and hydroxyl was also examined (Table S5, entries 4–7). The 1-phenyl-ethanol derivative with a halogen substituent at the para-position of the phenyl group (Table S5, entry 5) generated the corresponding aldehyde product in 78% yield. The reaction efficiency was affected by steric hindrance when a Cl group was located at the meta-position (Table S5, entry 6), which delivered a decreased aldehyde yield of 59% under standard reaction conditions. Notably, hydroxyl-substituted 1-phenyl-ethanol derivative (Table S5, entry 7) can be completely converted while affording 36% yield of aldehyde product. The relatively low yield is because the hydroxyl group easily causes a side reaction such as being oxidized to benzoquinone. Nevertheless, these data demonstrate the wide applications of Pt<sub>1</sub>/N-CNTs in electrocatalytic oxidative cleavage of the  $C_{\alpha}$ – $C_{\beta}$  bond in lignin model compounds. Moreover, the high recycling stability and reutilization of the Pt<sub>1</sub>/N-CNTs catalyst



was shown by carrying out the catalytic cleavage of lignin model compound **1a** five times without loss in catalytic activity (Figure S17). The content of Pt in the recovered Pt<sub>1</sub>/N-CNTs was determined to be 0.39 wt %, indicating no Pt leaching. EDX mapping and AC HAADF-STEM characterizations show that Pt atoms are still atomically dispersed with no aggregation observed (Figure S18), further corroborating the robust nature of the Pt<sub>1</sub>/N-CNTs catalyst.

**2.3. Mechanism Study of Electrocatalytic C<sub>α</sub>–C<sub>β</sub> Bond Cleavage.** We were intrigued about the mechanism of electrocatalytic C<sub>α</sub>–C<sub>β</sub> bond oxidative cleavage, as it has rarely been addressed in the literature.<sup>24,25</sup> A series of control experiments were conducted over the Pt<sub>1</sub>/N-CNTs catalytic system (Scheme S1). The ketone **2a** was hardly converted with very low yields of products under the standard reaction conditions (Scheme S1, eq 1), revealing that **2a** is not the intermediate for **1a** conversion. This phenomenon is in direct contrast to those found in conventional thermocatalytic systems,<sup>80–83</sup> where C<sub>α</sub>–OH was oxidized to C<sub>α</sub>=O prior to the C<sub>α</sub>–C<sub>β</sub> bond cleavage. Thus, a distinct reaction mechanism may take place in our electrocatalytic system. Phenyl formate as the other product of C<sub>α</sub>–C<sub>β</sub> bond cleavage was not detected in the reaction.<sup>84</sup> Further studies with phenyl formate as the substrate (Scheme S1, eq 2) indicate that it was unstable under reaction conditions, with considerable decomposition to phenol,<sup>85</sup> which illustrated the origin of phenol produced during this electrocatalytic reaction. Notably, the reaction was greatly inhibited when a radical scavenger, 2, 2, 6, 6-tetramethyl-1-piperidinyloxy (TEMPO)/butylated hydroxytoluene (BHT), was added into the reaction system (Scheme S1, eq 3), indicating the reaction proceeded via radical intermediates. An electron paramagnetic resonance (EPR) spin-trap technique was further employed to identify the generated radical species with 5,5-dimethyl-1-pyrroline N-oxide (DMPO) as the trapping agent. As shown in Figure S19, six EPR peaks can be clearly observed over Pt<sub>1</sub>/N-CNTs under the electrocatalytic conditions, indicating the formation of a carbon-centered radical intermediate during the electrocatalytic process.<sup>86</sup>

For an in-depth understanding of the catalytic mechanism of the C<sub>α</sub>–C<sub>β</sub> bond cleavage, the experiments with two deuterated substrates **1a'**–D and **1a''**–D were performed (Scheme S2). The substrate **1a'**–D with C<sub>α</sub>–D can be effectively converted as that of **1a**, meaning that C<sub>α</sub>–H oxidation is not the rate-determining step. Moreover, the presence of C<sub>α</sub>–D in deuterated aldehyde (Figure S22) indicates that the benzylic hydrogen is not scrambled or exchanged during the electrocatalytic C–C bond cleavage reaction. In contrast, the conversion of **1a''**–D with C<sub>β</sub>–D decreased dramatically compared with that of **1a**, indicating that C<sub>β</sub>–H abstraction is the rate-determining step for C<sub>α</sub>–C<sub>β</sub> bond cleavage. The cyclic voltammetry (CV) curves of Pt<sub>1</sub>/N-CNTs show that TBHP exhibited a lower onset oxidation potential of 0.20 V vs Ag/AgCl than that of **1a** (0.80 V vs Ag/AgCl) (Figure S20); thus, TBHP decomposed first prior to **1a** oxidation under the electrocatalytic conditions.

On the basis of the above results and literature reports,<sup>77,87</sup> the possible mechanism of electrocatalytic transformation of the lignin model molecule over Pt<sub>1</sub>/N-CNTs is proposed in Figure 4a. First, the *tert*-butoxyl radical (<sup>t</sup>BuO<sup>•</sup>) **A**<sub>1</sub><sup>•</sup> and *tert*-butyl peroxy radical (<sup>t</sup>BuOO<sup>•</sup>) **A**<sub>2</sub><sup>•</sup> are generated from TBHP<sup>77,88</sup> (1). Subsequently, C<sub>β</sub> radical **B**<sup>•</sup> is produced via C<sub>β</sub>–H abstraction of lignin model compound **1a** on the Pt<sub>1</sub>/N-

CNTs anode surface (2). It is noteworthy that the abstraction of a hydrogen atom to produce the radical intermediate to initiate C<sub>α</sub>–C<sub>β</sub> bond cleavage was also reported on the Ni(III) anode surface.<sup>24</sup> Lastly, <sup>t</sup>BuO<sup>•</sup>/<sup>t</sup>BuOO<sup>•</sup> reacts with the unstable C<sub>β</sub> radical **B**<sup>•</sup> to generate intermediate **C** via a radical/radical cross-coupling reaction (3). The reaction is followed by electron transferring in **C**,<sup>84</sup> inducing the cleavage of the C<sub>α</sub>–C<sub>β</sub> bond and the generation of aromatic aldehyde, phenol, and CO<sub>2</sub>.<sup>85</sup> H<sub>2</sub> is simultaneously produced at the cathode via H<sub>2</sub>O reduction.

To further investigate the detailed reaction mechanism of <sup>t</sup>BuOOH/**1a** activation and the radical cross-coupling reaction mentioned above, DFT calculations were also performed. The results are shown in Figure 4b. Two possible reaction pathways were proposed in this work. Within the <sup>t</sup>BuOO<sup>•</sup> pathway, <sup>t</sup>BuOOH dehydrogenates on the Pt<sub>1</sub>/N-CNTs surface, and the Gibbs reaction energy and energy barrier were calculated to be 1.24 and 1.53 eV, respectively. Within the chemisorption structure of **A**<sub>2</sub><sup>•</sup>+H<sup>\*</sup>, the hydrogen atom adsorbs on the C site of the Pt–N<sub>3</sub>C<sub>1</sub> center, and the adsorption energy was calculated to be 0.33 eV lower than that on the Pt site. For the H<sup>\*</sup> configuration (**A**<sub>2</sub><sup>•</sup>+H<sup>\*</sup>), the catalyst could be regenerated via the hydrogen evolution reaction, with the Gibbs reaction energy for this step calculated to be exothermic of –0.36 eV. After the formation of **A**<sub>2</sub><sup>•</sup> radical, the reaction is followed by **1a** dehydrogenation. The corresponding reaction energy and energy barrier were calculated to be 1.28 and 2.05 eV, respectively. The significant energy barrier and reaction energy reveal that **1a** direct dehydrogenation to form **B**<sup>•</sup> radical is the rate-determining step of this reaction pathway, and the apparent activation energy (*G*<sub>a</sub>) for this reaction pathway was calculated to be 3.56 eV. After the formation of **A**<sub>2</sub><sup>•</sup> and **B**<sup>•</sup> radicals, the reaction is followed by the radical coupling step to form the **C**<sub>2</sub> intermediate, and this step was calculated to be highly exothermic of –2.32 eV. The **C**<sub>2</sub> intermediate further forms the benzaldehyde, phenyl formate, and <sup>t</sup>BuOH products via one-step dissociation. The reaction was calculated to be highly exothermic of –3.08 eV, with a moderate energy barrier of 1.21 eV.

Additionally, we investigated the possible reaction pathway of <sup>t</sup>BuOOH dehydroxylation to <sup>t</sup>BuO<sup>•</sup> radical (**A**<sub>1</sub><sup>•</sup>). The reaction energy and energy barrier were calculated to be –0.12 and 0.63 eV, respectively. This shows that for the first step <sup>t</sup>BuOOH activation, it is much more favorable to form **A**<sub>1</sub><sup>•</sup> radical on the Pt<sub>1</sub>/N-CNTs catalyst. After the formation and desorption of **A**<sub>1</sub><sup>•</sup> radical, the reaction is then followed by **1a** dehydrogenation. In this step, the H atom from **1a** transfers to the OH<sup>\*</sup> on the surface to form H<sub>2</sub>O, and the **B**<sup>\*</sup> intermediate adsorbs on the Pt<sub>1</sub> site with the C–Pt bond length of 2.20 Å. The detailed structures for each elementary step are shown in Figure S21. The reaction energy and energy barrier for this step were calculated to be –0.51 and 0.44 eV, respectively. After the formation of **A**<sub>1</sub><sup>•</sup> and **B**<sup>•</sup> radicals, the reaction is followed by the radical coupling step to form the **C**<sub>1</sub> intermediate. This step was also calculated to be highly exothermic of –2.85 eV. The **C**<sub>1</sub> intermediate further forms the benzaldehyde, phenyl formate, and <sup>t</sup>BuH products via one-step dissociation. The reaction was calculated to be exothermic of –1.01 eV, with a moderate energy barrier of 0.56 eV. The apparent activation energy (*G*<sub>a</sub><sup>'</sup>) for this reaction pathway was calculated to be 1.57 eV. By comparing the two reaction

pathways, we are able to conclude that the  $^t\text{BuO}^\bullet$  pathway is much more favorable than the  $^t\text{BuOO}^\bullet$  pathway.

Remarkably,  $\text{C}_\alpha$  ketone<sup>13</sup> or  $\text{C}_\alpha$  radical intermediates<sup>89</sup> were usually involved in previously reported catalytic systems for **1a** oxidation. Both the two intermediates possess decreased bond dissociation energy (BDE) for  $\text{C}_\beta\text{--O}$  but increased BDE for the  $\text{C}_\alpha\text{--C}_\beta$  bond; thus, only  $\beta\text{--O--4}$  bond cleavage could be evoked while the  $\text{C}_\alpha\text{--C}_\beta$  bond remains intact. In contrast, the present  $\text{Pt}_1/\text{N-CNTs}$  electrocatalyst featured with the formation of the  $\text{C}_\beta$  radical intermediate, which is capable of coupling with  $^t\text{BuO}^\bullet$  to induce  $\text{C}_\alpha\text{--C}_\beta$  bond cleavage, is significantly distinguished from previously reported catalysts rendering its high selectivity for  $\text{C}_\alpha\text{--C}_\beta$  bond cleavage.

### 3. CONCLUSIONS

In summary, we present a new type of electrocatalyst for selective  $\text{C}_\alpha\text{--C}_\beta$  bond oxidative cleavage in lignin models, namely atomically dispersed  $\text{Pt}\text{--N}_3\text{C}_1$  sites anchored on N-doped CNTs. The electrocatalytic measurements suggest that  $\text{Pt}_1/\text{N-CNTs}$  possesses unprecedented high  $\text{C}_\alpha\text{--C}_\beta$  bond cleavage activity and selectivity, delivering 81% yield of benzaldehyde, which greatly exceeds previously reported electrocatalysts. Moreover,  $\text{Pt}_1/\text{N-CNTs}$  also demonstrates an overwhelming advantage over the state-of-the-art Pt electrode and Pt/C benchmark catalyst. Experimental mechanism investigation combined with DFT calculation suggests that the reaction proceeds via a key  $\text{C}_\beta$  radical intermediate, which facilitates the specific  $\text{C}_\alpha\text{--C}_\beta$  bond cleavage during the following radical/radical cross-coupling process. This work represents a significant advancement in developing high-performance and cost-effective catalysts for lignin degradation and valorization via the green and sustainable electrochemical route.

### ■ ASSOCIATED CONTENT

#### Supporting Information

The Supporting Information is available free of charge at <https://pubs.acs.org/doi/10.1021/jacs.1c02328>.

Experimental procedures for the preparation, characterization of materials, and the test of catalytic performances; details of DFT calculations; additional TEM, HAAD-STEM, physisorption, ICP-OES, Raman, XRD, XPS, XANES, EXAFS, EPR, and CV data; copies of  $^1\text{H}$  and  $^{13}\text{C}$  NMR spectra; data of recycling stability, substrate scope extension, and mechanism experiments for  $\text{Pt}_1/\text{N-CNTs}$ ; comparison of the catalytic performance of  $\text{Pt}_1/\text{N-CNTs}$  with previously reported thermocatalytic and photocatalytic systems for the oxidative cleavage of **1a** (PDF)

### ■ AUTHOR INFORMATION

#### Corresponding Authors

**Jiangwei Zhang** – Dalian National Laboratory for Clean Energy & State Key Laboratory of Catalysis, Dalian Institute of Chemical Physics, Chinese Academy of Sciences, Dalian 116023, China; [orcid.org/0000-0002-1221-3033](https://orcid.org/0000-0002-1221-3033); Email: [jwzhang@dicp.ac.cn](mailto:jwzhang@dicp.ac.cn)

**Haohong Duan** – Department of Chemistry, Tsinghua University, Beijing 100084, China; [orcid.org/0000-0002-9241-0984](https://orcid.org/0000-0002-9241-0984); Email: [hhduan@mail.tsinghua.edu.cn](mailto:hhduan@mail.tsinghua.edu.cn)

**Dingsheng Wang** – Department of Chemistry, Tsinghua University, Beijing 100084, China; [orcid.org/0000-0003-0074-7633](https://orcid.org/0000-0003-0074-7633); Email: [wangdingsheng@mail.tsinghua.edu.cn](mailto:wangdingsheng@mail.tsinghua.edu.cn)

#### Authors

**Tingting Cui** – Department of Chemistry, Tsinghua University, Beijing 100084, China

**Lina Ma** – State Key Laboratory of Chemical Resource Engineering, Beijing University of Chemical Technology, Beijing 100029, China

**Shibin Wang** – Institute of Industrial Catalysis, State Key Laboratory Breeding Base of Green-Chemical Synthesis Technology, College of Chemical Engineering, Zhejiang University of Technology, Hangzhou 310032, China

**Chenliang Ye** – Department of Chemistry, Tsinghua University, Beijing 100084, China; [orcid.org/0000-0002-0111-6748](https://orcid.org/0000-0002-0111-6748)

**Xiao Liang** – Department of Chemistry, Tsinghua University, Beijing 100084, China

**Zedong Zhang** – Department of Chemistry, Tsinghua University, Beijing 100084, China

**Ge Meng** – Department of Chemistry, Tsinghua University, Beijing 100084, China

**Lirong Zheng** – Beijing Synchrotron Radiation Facility, Institute of High Energy Physics, Chinese Academy of Sciences, Beijing 100049, China

**Han-Shi Hu** – Department of Chemistry, Tsinghua University, Beijing 100084, China; [orcid.org/0000-0001-9508-1920](https://orcid.org/0000-0001-9508-1920)

**Yadong Li** – Department of Chemistry, Tsinghua University, Beijing 100084, China; [orcid.org/0000-0003-1544-1127](https://orcid.org/0000-0003-1544-1127)

Complete contact information is available at: <https://pubs.acs.org/doi/10.1021/jacs.1c02328>

#### Author Contributions

<sup>†</sup>T.C., L.M., and S.W. contributed equally to this work.

#### Notes

The authors declare no competing financial interest.

### ■ ACKNOWLEDGMENTS

This work was supported by the National Natural Science Foundation of China (22005173, 21890383, 21871159, 21978147, 21935001), the China Postdoctoral Science Foundation (2019M660421), the National Key R&D Program of China (2018YFA0702003, 2020YFA0406101), and the Science and Technology Key Project of Guangdong Province of China (2020B010188002). We gratefully acknowledge the BL14W1 beamline of Shanghai Synchrotron Radiation Facility (SSRF), 1W1B beamline of Beijing Synchrotron Radiation Facility (BSRF), and BL11U beamline of the National Synchrotron Radiation Laboratory (NSRL) for providing beam time.

### ■ REFERENCES

- (1) Li, C.; Zhao, X.; Wang, A.; Huber, G. W.; Zhang, T. Catalytic transformation of lignin for the production of chemicals and fuels. *Chem. Rev.* **2015**, *115*, 11559–11624.
- (2) Jing, Y. X.; Dong, L.; Guo, Y.; Liu, X. H.; Wang, Y. Q. Chemicals from lignin: A review of catalytic conversion involving hydrogen. *ChemSusChem* **2020**, *13*, 4181–4198.
- (3) Zakzeski, J.; Bruijninx, P. C. A.; Jongerius, A. L.; Weckhuysen, B. M. The catalytic valorization of lignin for the production of renewable chemicals. *Chem. Rev.* **2010**, *110*, 3552–3599.



- (4) Xu, C.; Arancon, R. A. D.; Labidi, J.; Luque, R. Lignin depolymerisation strategies: towards valuable chemicals and fuels. *Chem. Soc. Rev.* **2014**, *43*, 7485–7500.
- (5) Liu, C.; Wu, S.; Zhang, H.; Xiao, R. Catalytic oxidation of lignin to valuable biomass-based platform chemicals: A review. *Fuel Process. Technol.* **2019**, *191*, 181–201.
- (6) Schmitt, D.; Regembrecht, C.; Hartmer, M.; Stecker, F.; Waldvogel, S. R. Highly selective generation of vanillin by anodic degradation of lignin: A combined approach of electrochemistry and product isolation by adsorption. *Beilstein J. Org. Chem.* **2015**, *11*, 473–480.
- (7) Bailey, A.; Brooks, H. Electrolytic oxidation of lignin. *J. Am. Chem. Soc.* **1946**, *68*, 445–446.
- (8) Hanson, S. K.; Baker, R. T.; Gordon, J. C.; Scott, B. L.; Thorn, D. L. Aerobic oxidation of lignin models using a base metal vanadium catalyst. *Inorg. Chem.* **2010**, *49*, 5611–5618.
- (9) Sedai, B.; Baker, R. T. Copper catalysts for selective C-C bond cleavage of  $\beta$ -O-4 lignin model compounds. *Adv. Synth. Catal.* **2014**, *356*, 3563–3574.
- (10) Mottweiler, J.; Puche, M.; Räuber, C.; Schmidt, T.; Concepción, P.; Corma, A.; Bolm, C. Copper- and vanadium-catalyzed oxidative cleavage of lignin using dioxygen. *ChemSusChem* **2015**, *8*, 2106–2113.
- (11) Lee, T. W.; Yang, J. W. Transition-metal-free conversion of lignin model compounds to high-value aromatics: scope and chemoselectivity. *Green Chem.* **2018**, *20*, 3761–3771.
- (12) Luo, H.; Wang, L.; Li, G.; Shang, S.; Lv, Y.; Niu, J.; Gao, S. Nitrogen-doped carbon-modified cobalt-nanoparticle-catalyzed oxidative cleavage of lignin  $\beta$ -O-4 model compounds under mild conditions. *ACS Sustainable Chem. Eng.* **2018**, *6*, 14188–14196.
- (13) Liu, S.; Bai, L.; van Muyden, A. P.; Huang, Z.; Cui, X.; Fei, Z.; Li, X.; Hu, X.; Dyson, P. J. Oxidative cleavage of  $\beta$ -O-4 bonds in lignin model compounds with a single-atom Co catalyst. *Green Chem.* **2019**, *21*, 1974–1981.
- (14) Pandey, M. P.; Kim, C. S. Lignin depolymerization and conversion: A review of thermochemical methods. *Chem. Eng. Technol.* **2011**, *34*, 29–41.
- (15) Bosque, I.; Magallanes, G.; Rigoulet, M.; Kärkäs, M. D.; Stephenson, C. R. Redox catalysis facilitates lignin depolymerization. *ACS Cent. Sci.* **2017**, *3*, 621–628.
- (16) Han, S.; Wang, C.; Wang, Y.; Yu, Y.; Zhang, B. Electrosynthesis of nitrate via the oxidation of nitrogen on tensile-strained palladium porous nanosheets. *Angew. Chem., Int. Ed.* **2021**, *60*, 4474–4478.
- (17) Möhle, S.; Zirbes, M.; Rodrigo, E.; Gieshoff, T.; Wiebe, A.; Waldvogel, S. R. Modern electrochemical aspects for the synthesis of value-added organic products. *Angew. Chem., Int. Ed.* **2018**, *57*, 6018–6041.
- (18) Tang, C.; Zheng, Y.; Jaroniec, M.; Qiao, S.-Z. Electrocatalytic refinery for sustainable production of fuels and chemicals. *Angew. Chem., Int. Ed.* **2021**, DOI: 10.1002/anie.202101522.
- (19) Zirbes, M.; Waldvogel, S. R. Electro-conversion as sustainable method for the fine chemical production from the biopolymer lignin. *Curr. Opin. Green Sustain. Chem.* **2018**, *14*, 19–25.
- (20) Ma, L.; Zhou, H.; Kong, X.; Li, Z.; Duan, H. An electrocatalytic strategy for C-C bond cleavage in lignin model compounds and lignin under ambient conditions. *ACS Sustainable Chem. Eng.* **2021**, *9*, 1932–1940.
- (21) Vasileff, A.; Zhu, Y.; Zhi, X.; Zhao, Y.; Ge, L.; Chen, H. M.; Zheng, Y.; Qiao, S.-Z. Electrochemical reduction of CO<sub>2</sub> to ethane through stabilization of an ethoxy intermediate. *Angew. Chem., Int. Ed.* **2020**, *59*, 19649–19653.
- (22) Du, X.; Zhang, H.; Sullivan, K. P.; Gogoi, P.; Deng, Y. Electrochemical lignin conversion. *ChemSusChem* **2020**, *13*, 4318–4343.
- (23) Garedew, M.; Lin, F.; Song, B.; DeWinter, T. M.; Jackson, J. E.; Saffron, C. M.; Lam, C. H.; Anastas, P. T. Greener routes to biomass waste valorization: Lignin transformation through electrocatalysis for renewable chemicals and fuels production. *ChemSusChem* **2020**, *13*, 4214–4237.
- (24) Pardini, V. L.; Smith, C. Z.; Utey, J. H. P.; Vargas, R. R.; Viertler, H. Electroorganic reactions. 38. Mechanism of electro-oxidative cleavage of lignin model dimers. *J. Org. Chem.* **1991**, *56*, 7305–7313.
- (25) Pardini, V. L.; Vargas, R. R.; Viertler, H.; Utey, J. H. Anodic cleavage of lignin model dimers in methanol. *Tetrahedron* **1992**, *48*, 7221–7228.
- (26) Rochefort, D.; Bourbonnais, R.; Leech, D.; Paice, M. G. Oxidation of lignin model compounds by organic and transition metal-based electron transfer mediators. *Chem. Commun.* **2002**, 1182–1183.
- (27) Cai, P.; Fan, H.; Cao, S.; Qi, J.; Zhang, S.; Li, G. Electrochemical conversion of corn stover lignin to biomass-based chemicals between Cu/Ni-Mo-Co cathode and Pb/PbO<sub>2</sub> anode in alkali solution. *Electrochim. Acta* **2018**, *264*, 128–139.
- (28) Wang, Y.-s.; Yang, F.; Liu, Z.-h.; Yuan, L.; Li, G. Electrocatalytic degradation of aspen lignin over Pb/PbO<sub>2</sub> electrode in alkali solution. *Catal. Commun.* **2015**, *67*, 49–53.
- (29) Zhang, Y. m.; Peng, Y.; Yin, X. l.; Liu, Z. h.; Li, G. Degradation of lignin to BHT by electrochemical catalysis on Pb/PbO<sub>2</sub> anode in alkaline solution. *J. Chem. Technol. Biotechnol.* **2014**, *89*, 1954–1960.
- (30) Lu, Z.; Tu, B.; Chen, F. Electro-degradation of sodium lignosulfonate. *J. Wood Chem. Technol.* **2003**, *23*, 261–277.
- (31) Parpot, P.; Bettencourt, A.; Carvalho, A.; Belgsir, E. Biomass conversion: Attempted electrooxidation of lignin for vanillin production. *J. Appl. Electrochem.* **2000**, *30*, 727–731.
- (32) Hao, X.; Quansheng, Y.; Dan, S.; Honghui, Y.; Jidong, L.; Jiangtao, F.; Wei, Y. Fabrication and characterization of PbO<sub>2</sub> electrode modified with [Fe(CN)<sub>6</sub>]<sup>3-</sup> and its application on electrochemical degradation of alkali lignin. *J. Hazard. Mater.* **2015**, *286*, 509–516.
- (33) Shao, D.; Liang, J.; Cui, X.; Xu, H.; Yan, W. Electrochemical oxidation of lignin by two typical electrodes: Ti/SbSnO<sub>2</sub> and Ti/PbO<sub>2</sub>. *Chem. Eng. J.* **2014**, *244*, 288–295.
- (34) Chang, X.; van der Zalm, J.; Thind, S. S.; Chen, A. Electrochemical oxidation of lignin at electrochemically reduced TiO<sub>2</sub> nanotubes. *J. Electroanal. Chem.* **2020**, *863*, 114049.
- (35) Tolba, R.; Tian, M.; Wen, J.; Jiang, Z.-H.; Chen, A. Electrochemical oxidation of lignin at IrO<sub>2</sub>-based oxide electrodes. *J. Electroanal. Chem.* **2010**, *649*, 9–15.
- (36) Reichert, E.; Wintringer, R.; Volmer, D. A.; Hempelmann, R. Electro-catalytic oxidative cleavage of lignin in a protic ionic liquid. *Phys. Chem. Chem. Phys.* **2012**, *14*, 5214–5221.
- (37) Wang, L.; Chen, Y.; Liu, S.; Jiang, H.; Wang, L.; Sun, Y.; Wan, P. Study on the cleavage of alkyl-O-aryl bonds by *in situ* generated hydroxyl radicals on an ORR cathode. *RSC Adv.* **2017**, *7*, 51419–51425.
- (38) Tian, M.; Wen, J.; MacDonald, D.; Asmussen, R. M.; Chen, A. A novel approach for lignin modification and degradation. *Electrochem. Commun.* **2010**, *12*, 527–530.
- (39) Rauber, D.; Dier, T. K.; Volmer, D. A.; Hempelmann, R. Electrochemical lignin degradation in ionic liquids on ternary mixed metal electrodes. *Z. Phys. Chem.* **2018**, *232*, 189–208.
- (40) Zhu, H.; Chen, Y.; Qin, T.; Wang, L.; Tang, Y.; Sun, Y.; Wan, P. Lignin depolymerization via an integrated approach of anode oxidation and electro-generated H<sub>2</sub>O<sub>2</sub> oxidation. *RSC Adv.* **2014**, *4*, 6232–6238.
- (41) Zhu, H.; Wang, L.; Chen, Y.; Li, G.; Li, H.; Tang, Y.; Wan, P. Electrochemical depolymerization of lignin into renewable aromatic compounds in a non-diaphragm electrolytic cell. *RSC Adv.* **2014**, *4*, 29917–29924.
- (42) Di Marino, D.; Stöckmann, D.; Kriescher, S.; Stiefel, S.; Wessling, M. Electrochemical depolymerisation of lignin in a deep eutectic solvent. *Green Chem.* **2016**, *18*, 6021–6028.
- (43) Jia, Y.; Wen, Y.; Han, X.; Qi, J.; Liu, Z.; Zhang, S.; Li, G. Electrocatalytic degradation of rice straw lignin in alkaline solution through oxidation on a Ti/SnO<sub>2</sub>-Sb<sub>2</sub>O<sub>3</sub>/α-PbO<sub>2</sub>/β-PbO<sub>2</sub> anode and reduction on an iron or tin doped titanium cathode. *Catal. Sci. Technol.* **2018**, *8*, 4665–4677.

- (44) Stiefel, S.; Marks, C.; Schmidt, T.; Hanisch, S.; Spalding, G.; Wessling, M. Overcoming lignin heterogeneity: reliably characterizing the cleavage of technical lignin. *Green Chem.* **2016**, *18*, 531–540.
- (45) Stiefel, S.; Schmitz, A.; Peters, J.; Di Marino, D. D.; Wessling, M. An integrated electrochemical process to convert lignin to value-added products under mild conditions. *Green Chem.* **2016**, *18*, 4999–5007.
- (46) Movil-Cabrera, O.; Rodriguez-Silva, A.; Arroyo-Torres, C.; Staser, J. A. Electrochemical conversion of lignin to useful chemicals. *Biomass Bioenergy* **2016**, *88*, 89–96.
- (47) Qiao, B.; Wang, A.; Yang, X.; Allard, L. F.; Jiang, Z.; Cui, Y.; Liu, J.; Li, J.; Zhang, T. Single-atom catalysis of CO oxidation using Pt<sub>1</sub>/FeO<sub>x</sub>. *Nat. Chem.* **2011**, *3*, 634–641.
- (48) Yang, J.; Li, W.; Wang, D.; Li, Y. Single-atom materials: small structures determine macroproperties. *Small Struct.* **2021**, *2*, 2000051.
- (49) Zhang, Z.; Feng, C.; Liu, C.; Zuo, M.; Qin, L.; Yan, X.; Xing, Y.; Li, H.; Si, R.; Zhou, S.; Zeng, J. Electrochemical deposition as a universal route for fabricating single-atom catalysts. *Nat. Commun.* **2020**, *11*, 1215.
- (50) Bai, S.; Liu, F.; Huang, B.; Li, F.; Lin, H.; Wu, T.; Sun, M.; Wu, J.; Shao, Q.; Xu, Y.; Huang, X. High-efficiency direct methane conversion to oxygenates on a cerium dioxide nanowires supported rhodium single-atom catalyst. *Nat. Commun.* **2020**, *11*, 954.
- (51) Kaiser, S. K.; Fako, E.; Manzocchi, G.; Krumeich, F.; Hauert, R.; Clark, A. H.; Safonova, O. V.; López, N.; Pérez-Ramírez, J. Nanostructuring unlocks high performance of platinum single-atom catalysts for stable vinyl chloride production. *Nat. Catal.* **2020**, *3*, 376–385.
- (52) Liu, K.; Zhao, X.; Ren, G.; Yang, T.; Ren, Y.; Lee, A. F.; Su, Y.; Pan, X.; Zhang, J.; Chen, Z.; Yang, J.; Liu, X.; Zhou, T.; Xi, W.; Luo, J.; Zeng, C.; Matsumoto, H.; Liu, W.; Jiang, Q.; Wilson, K.; Wang, A.; Qiao, B.; Li, W.; Zhang, T. Strong metal-support interaction promoted scalable production of thermally stable single-atom catalysts. *Nat. Commun.* **2020**, *11*, 1263.
- (53) Qiao, B.; Li, T.; Chen, F.; Lang, R.; Wang, H.; Su, Y.; Wang, A.; Zhang, T. Styrene hydroformylation with *in situ* H: Regioselectivity control by coupling with low-temperature water gas shift reaction. *Angew. Chem., Int. Ed.* **2020**, *59*, 7430–7434.
- (54) Xiong, Y.; Sun, W.; Han, Y.; Xin, P.; Zheng, X.; Yan, W.; Dong, J.; Zhang, J.; Wang, D.; Li, Y. Cobalt single atom site catalysts with ultrahigh metal loading for enhanced aerobic oxidation of ethylbenzene. *Nano Res.* **2021**, DOI: 10.1007/s12274-020-3244-4.
- (55) Zhang, J.; Zheng, C.; Zhang, M.; Qiu, Y.; Xu, Q.; Cheong, W.-C.; Chen, W.; Zheng, L.; Gu, L.; Hu, Z.; Wang, D.; Li, Y. Controlling N-doping type in carbon to boost single-atom site Cu catalyzed transfer hydrogenation of quinoline. *Nano Res.* **2020**, *13*, 3082–3087.
- (56) Zhang, N.; Ye, C.; Yan, H.; Li, L.; He, H.; Wang, D.; Li, Y. Single-atom site catalysts for environmental catalysis. *Nano Res.* **2020**, *13*, 3165–3182.
- (57) Zhang, Z.; Zhou, M.; Chen, Y.; Liu, S.; Wang, H.; Zhang, J.; Ji, S.; Wang, D.; Li, Y. Pd single-atom monolithic catalyst: Functional 3D structure and unique chemical selectivity in hydrogenation reaction. *Sci. China Mater.* **2021**, DOI: 10.1007/s40843-020-1579-7.
- (58) Zhou, L.; Martinez, J. M. P.; Finzel, J.; Zhang, C.; Swearer, D. F.; Tian, S.; Robotjazi, H.; Lou, M.; Dong, L.; Henderson, L.; et al. Light-driven methane dry reforming with single atomic site antenna-reactor plasmonic photocatalysts. *Nat. Energy* **2020**, *5*, 61–70.
- (59) Zuo, Q.; Liu, T.; Chen, C.; Ji, Y.; Gong, X.; Mai, Y.; Zhang, Y. Ultrathin metal-organic framework nanosheets with ultrahigh loading of single Pt atoms for efficient visible-light-driven photocatalytic H<sub>2</sub> evolution. *Angew. Chem., Int. Ed.* **2019**, *58*, 10198–10203.
- (60) Wang, L.; Xiao, M.; Zhang, L.; Luo, B.; Lyu, M.; Wang, Z.; Huang, H.; Wang, S.; Du, A. Molten salt mediated synthesis of atomic nickel co-catalyst on TiO<sub>2</sub> for improved photocatalytic H<sub>2</sub> evolution. *Angew. Chem., Int. Ed.* **2020**, *59*, 7230–7234.
- (61) Zhong, W.; Sa, R.; Li, L.; He, Y.; Li, L.; Bi, J.; Zhuang, Z.; Yu, Y.; Zou, Z. A covalent organic framework bearing single Ni sites as a synergistic photocatalyst for selective photoreduction of CO<sub>2</sub> to CO. *J. Am. Chem. Soc.* **2019**, *141*, 7615–7621.
- (62) Chen, Y.; Gao, R.; Ji, S.; Li, H.; Tang, K.; Jiang, P.; Hu, H.; Zhang, Z.; Hao, H.; Qu, Q.; Liang, X.; Chen, W.; Dong, J.; Wang, D.; Li, Y. Atomic-level modulation of electronic density of metal-organic frameworks-derived Co single-atom sites to enhance oxygen reduction performance. *Angew. Chem., Int. Ed.* **2021**, *60*, 3212–3221.
- (63) Lim, T.; Jung, G. Y.; Kim, J. H.; Park, S. O.; Park, J.; Kim, Y.-T.; Kang, S. J.; Jeong, H. Y.; Kwak, S. K.; Joo, S. H. Atomically dispersed Pt-N<sub>4</sub> sites as efficient and selective electrocatalysts for the chlorine evolution reaction. *Nat. Commun.* **2020**, *11*, 412.
- (64) Meng, X.; Ma, C.; Jiang, L.; Si, R.; Meng, X.; Tu, Y.; Yu, L.; Bao, X.; Deng, D. Distance synergy of MoS<sub>2</sub>-confined Rh atoms for highly efficient hydrogen evolution. *Angew. Chem., Int. Ed.* **2020**, *59*, 10502–10507.
- (65) Shan, J.; Ye, C.; Chen, S.; Sun, T.; Jiao, Y.; Liu, L.; Zhu, C.; Song, L.; Han, Y.; Jaroniec, M.; Zhu, Y.; Zheng, Y.; Qiao, S.-Z. Short-range ordered iridium single atoms integrated into cobalt oxide spinel structure for highly efficient electrocatalytic water oxidation. *J. Am. Chem. Soc.* **2021**, *143*, 5201–5211.
- (66) Wang, J.-G.; Liu, H.; Zhang, X.; Li, X.; Liu, X.; Kang, F. Green synthesis of hierarchically porous carbon nanotubes as advanced materials for high-efficient energy storage. *Small* **2018**, *14*, 1703950.
- (67) Xu, F.; Tang, Z.; Huang, S.; Chen, L.; Liang, Y.; Mai, W.; Zhong, H.; Fu, R.; Wu, D. Facile synthesis of ultrahigh-surface-area hollow carbon nanospheres for enhanced adsorption and energy storage. *Nat. Commun.* **2015**, *6*, 7221.
- (68) Wang, X.; Li, Y. Selected-control hydrothermal synthesis of  $\alpha$ - and  $\beta$ -MnO<sub>2</sub> single crystal nanowires. *J. Am. Chem. Soc.* **2002**, *124*, 2880–2881.
- (69) Cho, S. I.; Lee, S. B. Fast electrochemistry of conductive polymer nanotubes: Synthesis, mechanism, and application. *Acc. Chem. Res.* **2008**, *41*, 699–707.
- (70) Pan, L. J.; Pu, L.; Shi, Y.; Song, S. Y.; Xu, Z.; Zhang, R.; Zheng, Y. D. Synthesis of polyaniline nanotubes with a reactive template of manganese oxide. *Adv. Mater.* **2007**, *19*, 461–464.
- (71) Dresselhaus, M. S.; Dresselhaus, G.; Saito, R.; Jorio, A. Raman spectroscopy of carbon nanotubes. *Phys. Rep.* **2005**, *409*, 47–99.
- (72) Li, X.; Lin, B.; Li, H.; Yu, Q.; Ge, Y.; Jin, X.; Liu, X.; Zhou, Y.; Xiao, J. Carbon doped hexagonal BN as a highly efficient metal-free base catalyst for Knoevenagel condensation reaction. *Appl. Catal., B* **2018**, *239*, 254–259.
- (73) Li, Z.; Wang, C.; Chen, X.; Wang, X.; Li, X.; Yamauchi, Y.; Xu, X.; Wang, J.; Lin, C.; Luo, D.; et al. MoO<sub>3</sub> nanoparticles anchored on N-doped porous carbon as Li-ion battery electrode. *Chem. Eng. J.* **2020**, *381*, 122588.
- (74) Roy, S. S.; Papakonstantinou, P.; Okpalugo, T. I. T.; Murphy, H. Temperature dependent evolution of the local electronic structure of atmospheric plasma treated carbon nanotubes: Near edge x-ray absorption fine structure study. *J. Appl. Phys.* **2006**, *100*, 053703.
- (75) Kuznetsova, A.; Popova, I.; Yates, J. T.; Bronikowski, M. J.; Huffman, C. B.; Liu, J.; Smalley, R. E.; Hwu, H. H.; Chen, J. G. Oxygen-containing functional groups on single-wall carbon nanotubes: NEXAFS and vibrational spectroscopic studies. *J. Am. Chem. Soc.* **2001**, *123*, 10699–10704.
- (76) Park, J.; Lee, S.; Kim, H.-E.; Cho, A.; Kim, S.; Ye, Y.; Han, J. W.; Lee, H.; Jang, J. H.; Lee, J. Investigation of support effect in atomically dispersed Pt on WO<sub>3-x</sub> for high utilization of Pt in hydrogen evolution reaction. *Angew. Chem., Int. Ed.* **2019**, *58*, 16038–16042.
- (77) Horn, E. J.; Rosen, B. R.; Chen, Y.; Tang, J.; Chen, K.; Eastgate, M. D.; Baran, P. S. Scalable and sustainable electrochemical allylic C-H oxidation. *Nature* **2016**, *533*, 77–81.
- (78) Zhou, H.; Li, Z.; Xu, S.-M.; Lu, L.; Xu, M.; Ji, K.; Ge, R.; Yan, Y.; Ma, L.; Kong, X.; Zheng, L.; Duan, H. Selectively upgrading lignin derivatives to carboxylates through electrochemical oxidative C(OH)-C bond cleavage by a Mn-doped cobalt oxyhydroxide catalyst. *Angew. Chem., Int. Ed.* **2021**, *60*, 8976–8982.
- (79) Wang, M.; Lu, J.; Zhang, X.; Li, L.; Li, H.; Luo, N.; Wang, F. Two-step, catalytic C-C bond oxidative cleavage process converts

lignin models and extracts to aromatic acids. *ACS Catal.* **2016**, *6*, 6086–6090.

(80) Liu, M.; Zhang, Z.; Shen, X.; Liu, H.; Zhang, P.; Chen, B.; Han, B. Stepwise degradation of hydroxyl compounds to aldehydes via successive C-C bond cleavage. *Chem. Commun.* **2019**, *55*, 925–928.

(81) Liu, M.; Zhang, Z.; Song, J.; Liu, S.; Liu, H.; Han, B. Nitrogen dioxide catalyzed aerobic oxidative cleavage of C(OH)-C bonds of secondary alcohols to produce acids. *Angew. Chem., Int. Ed.* **2019**, *58*, 17393–17398.

(82) Zhao, L.; Shi, S.; Zhu, G.; Liu, M.; Gao, J.; Xu, J. Au-Pd alloy cooperates with covalent triazine frameworks for the catalytic oxidative cleavage of  $\beta$ -O-4 linkage. *Green Chem.* **2019**, *21*, 6707–6716.

(83) Tian, H.-R.; Liu, Y.-W.; Zhang, Z.; Liu, S.-M.; Dang, T.-Y.; Li, X.-H.; Sun, X.-W.; Lu, Y.; Liu, S.-X. A multicentre synergistic polyoxometalate-based metal-organic framework for one-step selective oxidative cleavage of  $\beta$ -O-4 lignin model compounds. *Green Chem.* **2020**, *22*, 248–255.

(84) Liu, H.; Li, H.; Lu, J.; Zeng, S.; Wang, M.; Luo, N.; Xu, S.; Wang, F. Photocatalytic cleavage of C-C bond in lignin models under visible light on mesoporous graphitic carbon nitride through  $\pi$ - $\pi$  stacking interaction. *ACS Catal.* **2018**, *8*, 4761–4771.

(85) Wang, M.; Li, L.; Lu, J.; Li, H.; Zhang, X.; Liu, H.; Luo, N.; Wang, F. Acid promoted C-C bond oxidative cleavage of  $\beta$ -O-4 and  $\beta$ -1 lignin models to esters over a copper catalyst. *Green Chem.* **2017**, *19*, 702–706.

(86) Li, H.; Qin, F.; Yang, Z.; Cui, X.; Wang, J.; Zhang, L. New reaction pathway induced by plasmon for selective benzyl alcohol oxidation on BiOCl possessing oxygen vacancies. *J. Am. Chem. Soc.* **2017**, *139*, 3513–3521.

(87) Hou, T.; Luo, N.; Li, H.; Heggen, M.; Lu, J.; Wang, Y.; Wang, F. Yin and yang dual characters of CuO<sub>x</sub> clusters for C-C bond oxidation driven by visible light. *ACS Catal.* **2017**, *7*, 3850–3859.

(88) Liu, W.; Li, Y.; Liu, K.; Li, Z. Iron-catalyzed carbonylation-peroxidation of alkenes with aldehydes and hydroperoxides. *J. Am. Chem. Soc.* **2011**, *133*, 10756–10759.

(89) Wu, X.; Fan, X.; Xie, S.; Lin, J.; Cheng, J.; Zhang, Q.; Chen, L.; Wang, Y. Solar energy-driven lignin-first approach to full utilization of lignocellulosic biomass under mild conditions. *Nat. Catal.* **2018**, *1*, 772–780.